Multiscale characterization of chemical-mechanical interactions between polymer fibers and cementitious matrix

Daniel Hernández-Cruz,[a,b]

Craig Hargis[b]

Sungchul Bae[b]

Pierre A. Itty[b]

Cagla Meral[b]

Jolee Dominowski[c]

Michael J. Radler[c]

David A. Kilcoyne[d]

Paulo J.M. Monteiro[b,*]

[a]Faculty of Engineering, Universidad Autónoma de Chiapas, Tuxtla Gutiérrez, Chiapas, Mexico

[b]Department of Civil and Environmental Engineering, University of California, Berkeley, CA, USA

[c]Dow Construction Chemicals, Midland, Michigan, USA

[d]Advanced Light Source-Lawrence Berkeley National Laboratory, Berkeley, CA, USA

*Corresponding author: Tel.: +1 (510) 643-8251; Fax: +1 (510) 643-8928; E-mail address: monteiro@ce.berkeley.edu; Department of Civil and Environmental Engineering, 725 Davis Hall, University of California, Berkeley, CA 94720-1710, USA

Abstract

Together with a series of mechanical tests, the interactions and potential bonding between polymeric fibers and cementitious materials were studied using scanning transmission X-ray microscopy (STXM) and microtomography (μCT). Experimental results showed that these techniques have great potential to characterize the polymer fiber-hydrated cement-paste matrix interface, as well as differentiating the chemistry of the two components of a bi-polymer (hybrid) fiber – the polypropylene core and the ethylene acrylic acid copolymer sheath. Similarly, chemical interactions between the hybrid fiber and the cement hydration products were observed, indicating the chemical bonding between the sheath and the hardened cement paste matrix. Microtomography allowed visualization of the performance of the samples, and the distribution and orientation of the two types of fiber in mortar. Beam flexure tests confirmed improved tensile strength of mixes containing hybrid fibers, and expansion bar tests showed similar reductions in expansion for the polypropylene and hybrid fiber mortar bars.

Keywords: Reinforcing Concrete Fiber, STXM, μCT, hybrid fiber, NEXAFS.

1. Introduction

Extending the service life of reinforced concrete structures and reducing maintenance costs is one approach in the quest to improve the sustainability of the current infrastructure. For this purpose, different types of organic or carbon-based materials, such as polymers in both fiber or in aqueous forms, are used to improve the toughness and durability of concrete [1-5]. Polymers that have been used in aqueous or emulsion form include the following: styrene acrylate (SA), vinylpropionate and vinylidene chloride (VVC), acrylate with a coupling agent (ACA) [1,2], polyethylene and vinylacetate (EVA or LATEX) [3,4]. Polymers used in the fiber form include polypropylene (PP) [5,6],

polyacrylonitrile (PAN) [7], polyethylene (PE), polyvinyl alcohol (PVA) [8], nylon [9], and carbon fibers [10].

The diversity of such applied materials is because different polymers exhibit better bonding characteristics to cementitious material compared to others. For instance, the hydrophobic surface of polypropylene (PP) does not adhere satisfactorily to the cementitious matrix [13, 14]; therefore, additional research has been conducted to search for more hydrophilic materials or surfaces that could improve the bonding of the fiber with the hardened cement paste (HCP). Peled et al. [15] tested and suggested the surface treatment of PP fibers by chemical and mechanical treatments. For chemical treatments, they suggested porofication, surface-active agents (detergent), purification, and surface treatment with polyvinyl acetate (PVAc) or sulfuric acid-dichromate. Mechanical treatment involved rubbing or crimping the fibers. With the exception of PVAc and crimping treatments, the rest of the treatments effectively improved either first crack stress or post-cracking behavior, or both. Pereira et al. [16] used hybrid fibers (blends; HybPAN: 1% PVA + 1% PAN, and HybPP: 1% PVA + 1.25 PP) with the goal of producing a more reactive or active polymer surface, in order to improve the material's bonding and therefore the mortar or concrete performance. Most research on blended fibers has focused on producing hybrid polymers; they are cost-effective to produce and lend themselves to surface treatment, without losing tensile strength. In addition, Pereira et al. [16] and Blunt et al. [17] used different conventional and hybrid fibers to improve concrete's mechanical properties and reduce its weight. A hybrid fiber is obtained by blending different polymers, creating multilayers, or modifying the fiber surface by any means, in order to improve bonding when embedded in a cementitious matrix.

The mechanical property benefits of fiber reinforcement include improvements in crack resistance, strength, toughness, impact energy absorption, increased abrasion resistance, ductility, and dimensional stability. Most of these improvements occur when a proportioned mixture of polymer fibers and steel fibers are used [2,5-10,12,18], as confirmed by Banthia et al. [19,20]. Banthia et al. also demonstrated that polymer fibers are effective as microcrack expansion reducers and improve early age mechanical properties. Currie et al.[13] and Bentur et al. [14] studied the interaction between PP fibers and

cementitious materials, and showed how the fibers control crack propagation in fiber reinforced concrete, including pull out and rupture with the surrounding HCP (see Larson et al. [10], and Xu et al. [11] for further discussion on this mechanism). Also, Felekoglu et al. [12] investigated how gas plasma surface-modified fibers, such as polyvinylbutane (PVB), PP, or PVA, can improve the mechanical performance of concrete composites. Such modifications improved the interface adhesion and frictional bond between the fibers and the cement matrix.

In addition to improving the concrete´s structural properties at early ages, polymer fibers also improve concrete´s durability. It is well known that chemical or physical effects can decrease the strength or mechanical properties in mortars and concrete. Factors such as temperature, water, salt ingress (i.e., chlorides), and carbonation of the concrete cover contribute to corrosion of the reinforcement steel and cracking of the concrete surrounding the corroded reinforcement. Other effects such as expansion, cracking, and fracture contribute to the degradation as well, even more when alkali-silica reactive aggregate is used. Alkali-silica reaction (ASR) promotes cracks in the concrete; the cracks then accelerate the ingress of deleterious agents down to the reinforcement surface, accelerating corrosion and prematurely damaging the structure. In order to reduce these effects, polymer and steel microfibers have been suggested to reduce the microstructure degradation and enhance the concrete durability [18,23]. Among those materials, reinforced polymer composites [23] and aqueous epoxy mixed during the concrete preparation minimized the ASR and decreased the concrete deterioration [24]. Although the previously mentioned studies utilized conventional characterization techniques such as scanning electron microscopy (SEM) and transmission electron microscopy (TEM), none of them help to properly identify the chemical composition and the combined chemical interface properties of the material attached to the polymer fibers and the cementitious bulk.

Synchrotron based x-ray microscopy has been useful in observing *in situ* hydration of cementitious systems [25-27]. Silva et al. [27] demonstrated how aqueous polymers influence the hydration process of cementitious materials; however, these *in situ* X-ray microscopy experiments were not able to simultaneously characterize the elements participating in the reactions. In the last decade, scanning transmission X-ray microscopy

(STXM), a technique based on synchrotron radiation, began to be used as a tool for cementitious materials studies [30]. STXM captures images at different electron binding energies and provides near-edge X-ray absorption fine structure (NEXAFS) spectra, which help to determine the chemical composition of the material under examination. Moreover, STXM can combine or correlate a series of morphology images at specific spectral energies in order to obtain chemical spatial mapping of elements (functional groups) involved in the material. Ha et al. [28] showed the possibility of determining each of the elements present in a polymer modified C-S-H.

This investigation studies the interaction at the interface between the HCP and a relatively new hybrid (bi-component) fiber proposed by Reddy et al. [29], composed of an ethylene acrylic acid copolymer (EAA) coaxially extruded with PP fiber core, and a monofilamented PP fiber. The study utilized STXM to determine chemical information about the fiber/HCP interface, and microtomography (μCT) to better understand the fiber distribution *in situ*. Additionally, the fibers' ability to control expansion due to ASR and flexure response was determined, thereby clarifying how an improved fiber-to-matrix bond affects the mechanical response of the composite.

2. Materials and Methods

2.1. Materials

The hybrid fiber (approx. 17 μm in diameter and 18 mm long) is composed of an ethylene acrylic acid copolymer (EAA ~1.7 μm), coaxially extruded with PP fiber core (15 μm in diameter), see Fig. 1. Because of its carboxyl functional groups, the EAA sheath is expected to act as a reactive layer, enhancing the adhesion or bonding between the reinforcing polymer PP fiber and the cement matrix. In addition, a monofilament PP fiber (approx. 50 μm in diameter and 13 mm long) was used. Both fibers and raw material in pellet from were provided by The Dow Chemical Company (DOW®). ASTM Type I cement was utilized.

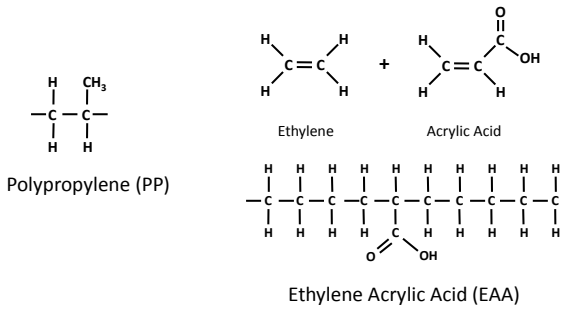

Fig. 1: Molecular structure of PP, EAA, and monomers ethylene and acrylic acid.

2.2. Scanning Transmission X-ray Microscopy

In order to obtain reference spectra of the fibers, the hybrid and the monofilament fiber were embedded in epoxy and then sectioned to less than 150 nm by using an Ultracut-E Reichert-Jung microtome. The sections were placed on a Cu TEM grid for analysis by STXM at the Advanced Light Source (ALS). Cement paste/fiber composite specimens were prepared and cast into 2.54 × 2.54 cm plastic cylinders, and cured for 7 and 28 days. The water to cement ratio (w/c) was set to 0.5, and the volume of fibers was 1%. After 7 or 28 days of curing at 21ºC and 100% R.H., the cylinders were dried in a dessicator in vacuum for 12 hrs and then were sliced using a diamond saw in order to obtain slices 1 mm thick or less.

From these slices, two types of samples were prepared. In the first case, the slices were directly embedded in epoxy and then microtomed. In the second case, the slices were crushed in order to remove most of the cement matrix, leaving the fiber almost bare with only a few cement paste matrix particles attached to its surface. In both cases, the samples were microtomed between 200 and 500 nm thick. These slices were placed on Cu TEM grids for further analysis by STXM. Because of the brittleness of the HCP, it was not possible to obtain microtome samples thinner than 200 nm which contained fiber embedded in the cement matrix.

Beamlines 5.3.2.1 and 5.3.2.2 STXM at the ALS, operate at energies ranging from 700 to 2200 eV, and from 270 to 800 eV, respectively. A spectral resolution of 0.1 eV was used to determine the chemical bonding at the interface between the fibers and the cement matrix at a spatial resolution of ~30 nm on both instruments. The software aXis2000 [32] was used for spectrum and image processing.

STXM can provide the user with four types of data: a) A single absorption image taken at any specified energy (eV) within the desired energy edge, (i.e., for C K, between 280 and 320 eV; Ca L, between 340 and 365 eV; Al K, between 1550 and 1600 eV, and Si K, between 1820 and 1860 eV). The single absorption images can then be converted to optical density (OD) by applying the Beer-Lamber law: $OD = \ln [I_1 / I_0]$, where I_1 is the intensity of the radiation through the material, and I_0 is the incident radiation. When taking single images, one can perform an OD two-image map, which is obtained by the simple equation $C = -\ln(B/A)$, where A is an image taken at a pre-edge energy, and B is an image taken at a strong peak absorption or at some intermediate energy. This process attenuates dominant contributions to better visualize less intense signals, enhancing features where a specific functional groups and associated elements are located and distributed. b) Point spectra consist of measuring one or multiple spectra at a different region of interest (ROI) on the sample. c) Line scans measurements of a NEXAFS spectra at every single pixel along a line across the sample in the chosen spectral range. d) Images (stacks) measured at one or multiple regions in the sample, at every single energy in the chosen spectral range so that each voxel-pixel contains a full NEXAFS spectra.

After extracting the spectra from the line scan or the image stack, a single value decomposition (SVD) analysis on the image stack can be evaluated, to obtain component image mapping. The SVD will perform a convolution between every selected spectrum (i.e., corresponding to three elements in the sample, for example) and every single pixel from the image stack, thereby obtaining images related to every element for which a spectra was obtained with a standard deviation reflecting the processing error. Post-analysis of the images can then be combined to produce a Red-Green-Blue (RGB) composite image, showing the distribution of the elements/functional groups in the sample at specific energies.

2.4. Mechanical and Durability Tests

To determine the fibers' response in an accelerated ASR environment, a modified version of ASTM C 1260 was utilized [34]. The test was modified by using the finer sand gradation and lower temperature to match the conditions used for the μCT samples (38.5% 0.60-1.18 mm, 38.5% 0.30-0.60 mm, and 23% 0.15-0.30 mm). This gradation corresponds to the smallest three aggregate sizes specified by ASTM C 1260 renormalized to 100%. The w/c ratio was set to 0.47, a sand-to-cement ratio of 2.25, and a fiber volume of 1% when mixes contained fibers. Three specimens of size 2.54 × 2.54 × 27.94 cm (1 in. × 1 in. × 11 in.) were prepared for each of the three mixes (a control sample without fibers, a second sample containing PP fibers, and the third sample composed of hybrid fibers).

Flexure tests were carried out using third-point loading according to ASTM C 1609 [35]. Two control, two PP, and two hybrid mortar beams 7.62 × 7.62 × 27.94 cm (3 in. × 3 in. × 11 in) were prepared and tested after 28 days of curing at 21°C and 100% R.H. The mix design parameters were similar to those used for the expansion tests; however, the sand gradation had a fineness modulus of 2.9.

2.5. Microtomography

Mortar composite cylinders, of 7 mm diameter and length 3 cm, were fabricated to accomodate the transmitted X-rays and to facilitate mounting into the microtomography's three-jaw chuck. Three cylinders were prepared, the control (without fibers), one containing PP fibers, and one containing hybrid fibers. The hybrid fibers were cut to ~5mm so they could fit along the cylinder's transverse direction. Samples contained a w/c of 0.47 and a sand-to-cement ratio of 2.25; when fibers were incorporated, a fiber volume ratio of 1% was used.

Previous research confirmed that the sand, utilized in this study, to be reactive [33]. To better accommodate the small molds and to not dominate the μCT field of view with aggregates, a sand gradation as specified above was used. The sealed samples were demolded after curing for 24 hours at 21°C, and then stored in 50 ml of 1 M NaOH solution at 50°C for 130 days; 50°C was used as the curing temperature to accelerate the ASR without approaching the fiber's melting temperature. The samples were then observed

periodically using hard X-ray μCT, which was performed at beamline 8.3.2 utilizing an X-ray beam with an energy of 38 keV at a ring current of 500 mA. A PCO.edge sCMOS camera (2560x2160 pixels) was used with a 2x lens, giving a 3.25 μm pixel size with up to 8.3 mm field of view. This resolution facilitated the study of the microstructural behavior and fiber orientation and distribution. A total of 1025 images were captured (~2 mm-thick section), reconstructed using the software Octopus® [36], and visualized with FIJI [37]. The final 3D rendering and segmentation was performed with Avizo [38].

3. Results and Discussion

3.1. Spectro-microscopic Analysis

3.1.1. Analysis of the fibers

The C K-edge NEXAFS measured on microtomed PP and EAA pellets are shown in Fig. 2. These spectra are similar to those reported by Dhez et al. [31] for PP. The main difference between the PP and the EAA spectra is the doublet appearing around 287.7 eV in the EEA spectra. The doublet is due to the carboxyl groups of the EAA polymer. Carboxyl groups are hydrophilic, making the material more reactive with the Ca ions from the cement paste, as discussed below. The bump around 285.2 eV is due to radiation damage.

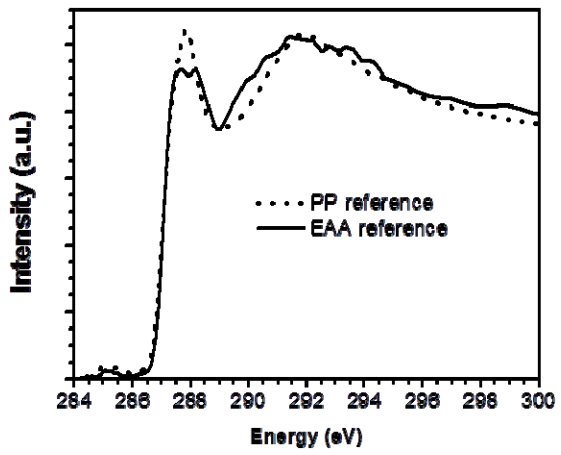

Fig. 2: C K-edge NEXAFS spectrum from the different polymer materials analyzed under STXM.

Particular attention to the details of the samples at the meso scale is needed to characterize the interface between the core (PP) and the sheath (EAA). Fig. 3 shows STXM OD images from the two types of fibers that were embedded in epoxy, as described earlier. In Fig. 3b, the EAA sheath (~1.7μm) can easily be distinguished from the PP core. The white bordered rectangular ROI depict the areas where the C K-edge NEXAFS was recorded.

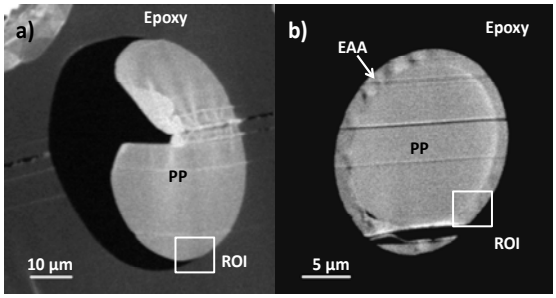

Fig. 3: STXM OD images of (a) the PP fiber taken at 287.7 eV and (b) the hybrid fiber taken at 288.2 eV.

The C K-edge image stack shown in Fig. 4a was taken from the ROI shown in Fig. 3b. Fig. 4a shows the extracted spectra from three regions corresponding to the epoxy, EAA sheath, and PP fiber core. A singular value decomposition (SVD) analysis results in the RGB composite image map shown in Fig. 4b. The composite image clearly shows that the three different components can be differentiated via spectromicroscopy. The green-bluish areas by the sheath-epoxy interface are due to the wrinkles present in the material made during the microtome sectioning, which could be misinterpreted as a density or chemical change.

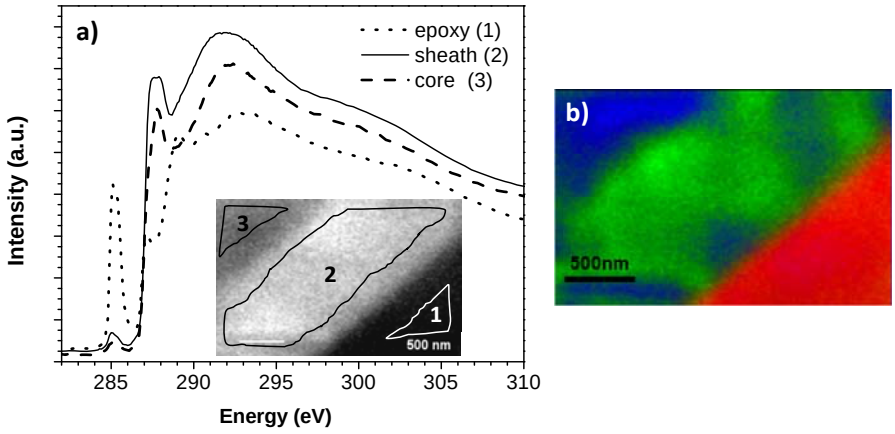

Fig. 4: (a) Spectrum of the three different components extracted C K-edge image stack from the ROI depicted in Fig. 3b (see inset): epoxy (dotted line), EAA sheath (solid line), and PP core (dashed line); and (b) the RGB composite image map showing the differentiation of the polymers, PP core (blue), EAA sheath (green), and epoxy (red).

3.1.2. Polymer fibers embedded in a cement paste matrix

Two approaches were considered when analyzing the embedded fiber in the HCP. In the first case, the samples were obtained by sectioning the embedded fiber in the HCP; results are shown in Figs. 5–7, where the optical density (OD) images taken at the Ca L and Si K-edge are presented. Because microtome sectioning of a brittle material such as HCP is problematic, a second approach was also investigated. In Figs. 8–9, results from the fibers sectioned from crushed samples with either hybrid or PP fibers are presented.

Ca L-edge (349.1 eV) and Si K-edge (1847.7 eV) OD images of a hybrid fiber in HCP embedded in epoxy matrix are shown in Fig. 5a-b. Unhydrated cement particles rich in Ca and Si are marked with higher intensities and are brighter than the hydrated cement phases. A rim corresponding to the EAA sheath (note arrows) appears at the Ca edge, suggesting Ca absorption.

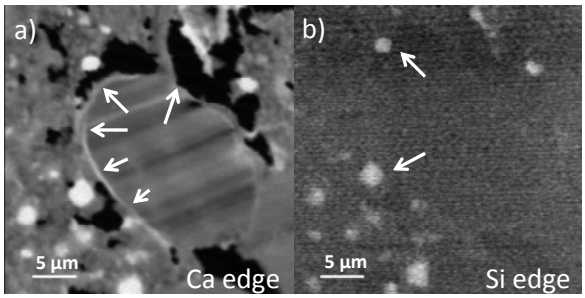

Fig. 5: Optical density (OD) images of a hybrid fiber in HCP embedded in epoxy (a) at Ca peak (at 349.1 eV), and (b) at Si peak, (at 1847.7 eV). The arrows on (a) indicate the sheath area around the fiber core containing traces of Ca, while on (b) they indicate the unhydrated cement particles rich in Si.

Fig. 6 shows a second site with an interface between the hybrid fiber and the HCP. A spectral line scan measured at the Ca L-edge from the fiber core to the HCP shows a spatial distribution that is specific to the components present in the compositite. The line scan can be divided into four regions (Fig. 6b), and NEXAFS spectra extracted. Regions indicated as 2 and 3 can be identified as the EAA sheath. The difference resides on the stronger Ca peaks (around 349.1 and 352.5 eV) found in region 3, indicating the Ca migration or diffusion into the EAA sheath from the HCP; no trace of Ca can be observed in the PP core fiber (region 1) or the epoxy matrix (region 4). The brightness of the region near the top of the line scan OD image (Fig. 6c) is due to the high Ca content and can be attributed to the unhydrated cement phase found near the end of the arrow in Fig. 6b.

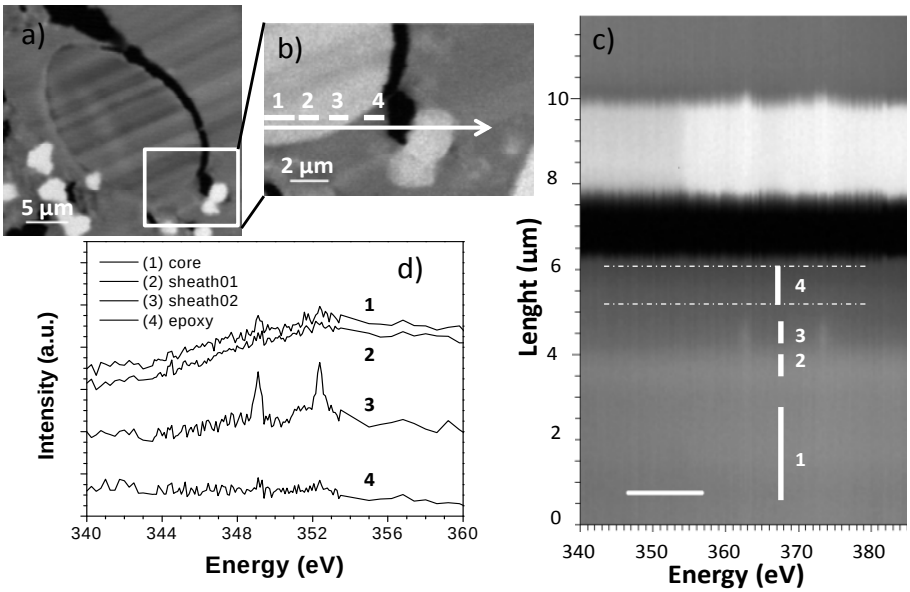

Fig. 6: (a) an OD image showing the area where a line scan at Ca L edge was performed; (b) a zoomed in image showing the line scan position and the four regions where the NEXAFS spectra were extracted; (c) a line scan image showing the four regions where the spectra was extracted; and (d) the four extracted NEXAFS spectra.

A similar case is depicted in Fig. 7 where instead of performing a line scan, an image stack was carried out. Fig. 7c shows the three regions where Ca L-edge NEXAFS spectra were extracted and used to obtain a RGB composite image (Fig. 7d). Focusing on the sheath spectra (solid line), note that there are two characteristic Ca peaks identifying the region as Ca-rich, enhanced in green in Fig. 7d. In contrast, the spectra from the core (dashed line) show only a trace of Ca. Again, the Ca detected in the sheath (region 2) suggests bonding or interaction between the EAA sheath and the HCP. However, a correlation to a specific Ca compound, such as $Ca(OH)_2$, which is the most common material found at the surface of polymeric fibers embedded in cementitious materials [9,14,15], remains to be proven.

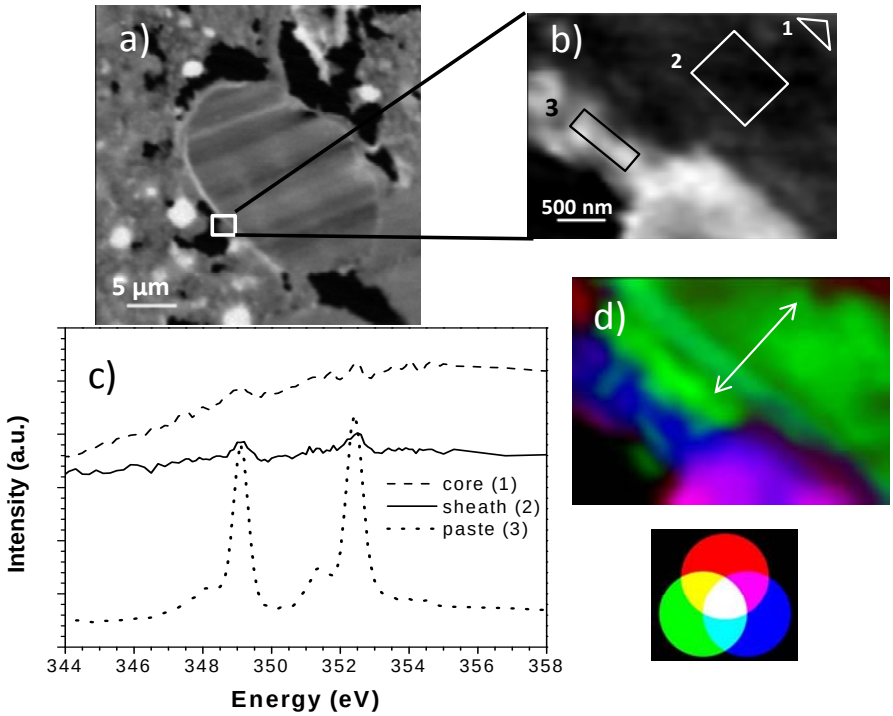

303

304 Fig. 7: (a) an OD image showing the area where a Ca image stack was obtained; (b) the OD
305 image extracted from the image stack showing the three areas where the NEXAFS spectra
306 were extracted (c) the NEXAFS spectra extracted for the three areas representing the PP
307 core (1), the EAA sheath (2), and the clear and strong spectra of the HCP area (3); and (d)
308 the RGB composite map showing the PP core in red, the EAA sheath in green, and the HCP
309 in blue.

310

311 A hybrid fiber (Fig. 8a), obtained from a crushed HCP composite was used to
312 perform a Ca L-edge stack on the indicated ROI. The fiber was, unfortunately, ripped
313 during sectioning with the microtome, and a gap formed between the PP and the sheath;
314 with the sheath the material that remained bonded with epoxy. Fig. 8b shows an image
315 taken at 349.1 eV from where Ca L-edge spectra were extracted (Fig. 8c). No Ca was
316 identified on the spectra extracted from the epoxy area, only on the sheath area.

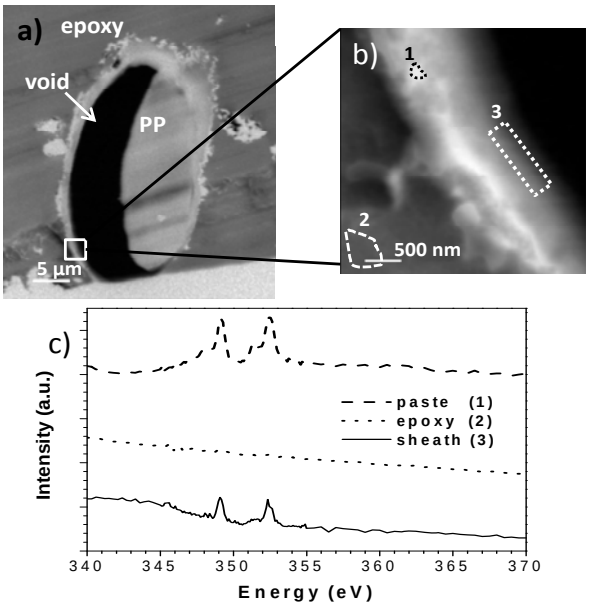

317

318 Fig. 8: (a) an OD image showing a hybrid fiber obtained from a crushed piece of composite
319 paste where the ROI indicates the location from which a Ca L edge image stack was
320 obtained; (b) the OD image extracted from the image stack (at 349.1 eV) showing the three
321 areas where the NEXAFS spectra was extracted; and (c) NEXAFS spectra extracted for the
322 three areas representing the Ca rich particle (1) from the HCP paste, the epoxy (2), and the
323 EAA sheath (3).

324

325 As shown in Fig. 9, a STXM analysis of a PP fiber obtained from a crushed HCP
326 composite was performed. Two ROI (see Fig. 9a) were selected in order to perform an
327 image map (Fig. 9b) and a Ca L-edge image stack (Fig. 9d). The image map was performed
328 (Fig. 9c) at the same area as Fig. 9b; no Ca was found at the interface (indicated by the
329 arrows) with the PP fiber. Although unhydrated cement paste particles close to the
330 interface, on the epoxy side, but none bonded to the PP fiber is visible. Ca NEXAFS
331 spectra (Fig. 9e) were extracted from the areas indicated in Fig. 9d. Here, no change in the
332 absorption signal is found on either of the two spectra (indicated as core and edge),
333 confirming the absence of Ca at the interface of the PP fiber with the HCP and therefore the
334 weak bonding between the two.

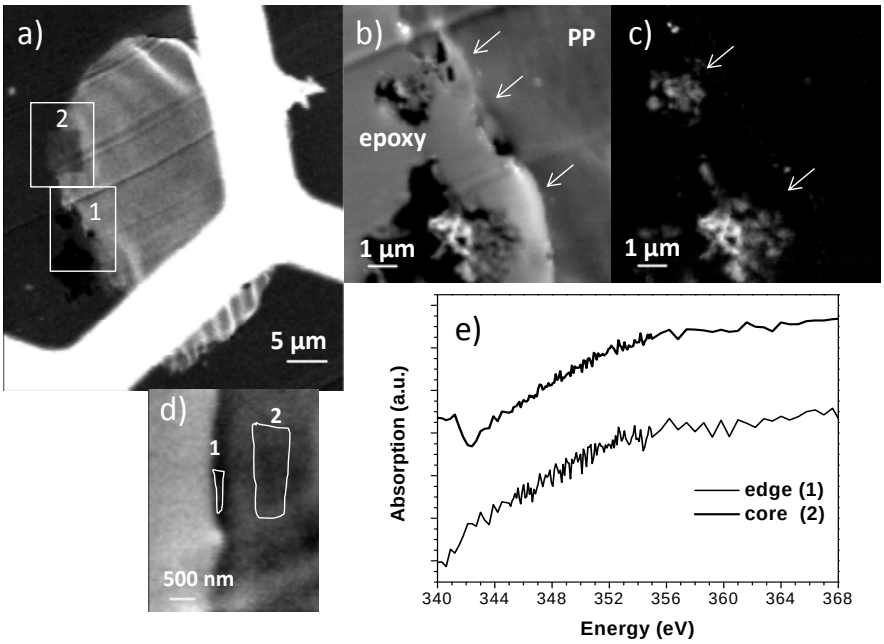

335

336 Fig. 9: (a) An OD image of a PP fiber from a crushed piece of composite paste where the
337 ROI indicates the areas where an image map and a Ca image stack were obtained; (b) an
338 OD image at Ca L edge, at a strong energy absorption (349.1 eV); (c) an image map
339 obtained from the same area as (b); and (d) an absorption image from the image stack from
340 ROI-2 where two absorption spectra were extracted and shown in (e).

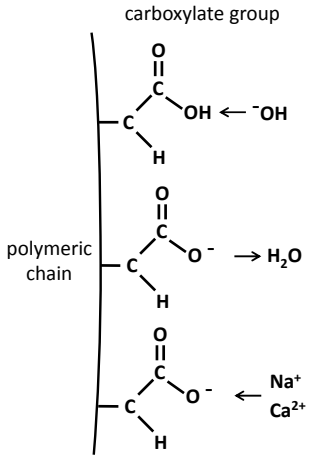

341

Fig. 10: Molecular structure of the carboxylate bonding.

According to these results, it appears that the carboxylate groups (depicted in Fig. 10) from the EAA sheath are deprotonated by the hydoxyl ions from the cement paste. The negatively charged oxygen of the carboxylate group then attracts cations from the paste such as Ca^{2+} or Na^{+}. The bonding between the carboxylate groups of the EAA sheath and the calcium from the cement paste allow the fibers to improve the bonding with the cement paste matrix.

3.2. Mechanical analysis

Three types of studies were performed in order to investigate the mechanical and structural behavior of composites. The first study conducted was the expansion bar test, the second was the μCT, and the third was the flexure test. The μCT investigated the distribution and orientation of the embedded fibers in the cement matrix at the micro-scale level. In the case of the expansion and the flexure tests, the structural behavior (the ability to restrain expansion, toughness, and stabilized post cracking load) of polymer fiber reinforced mortar specimens was compared.

3.2.1. Expansion bars tests

Fig. 11 shows the results from expansion bar tests. Both sets of expansion bars with fibers showed reductions in expansion compared to the control without fibers. However, no significant performance difference was observed between the expansion bars with hybrid fibers compared to those samples containing PP fibers. Additionally, the μCT results show that significant amounts of air entrapped in the mixes containing fibers. Air void systems have been shown to reduce—or at least delay—expansion caused by ASR due to the gels escaping to the air voids and relieving or avoiding the pressures that can develop from ASR gel formation. Indeed, in the bottom right corner of Fig. 12d, an air void can be observed

that is filled with ASR gel (see dashed circle). Consequently, it is difficult to describe the reduction in expansion being restrained as a result of the incorporation of the fibers, or attributed to a reduction in the swelling pressures that result from gel escaping into the distributed air voids. Future studies that investigate the use of fibers to ameliorate ASR expansion should test the mixes for air content to determine if any reduction in expansion could be attributed to the inclusion of fibers or is in fact a result of differences in air content.

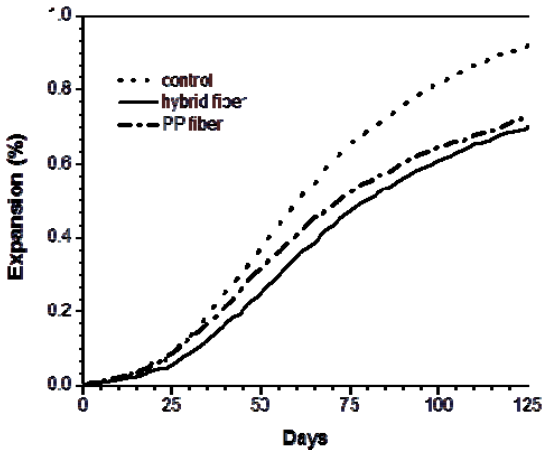

Fig. 11: Expansion of mortar bars due to ASR for three types of specimens: the control sample without fibers, the sample containing PP, and the sample containing hybrid fibers.

3.2.2. Microtomography analysis

Figs. 12a to 12d show tomographic images taken from the PP and hybrid mortar composites under control after being submerged in a 1M NaOH solution for 1 day and 74 days (for the hybrid composite) and 9 days and 84 days (for the PP composite). Early and late ASR attack occurrs: reactive aggregates dissolve and nearby pores are filled with hygroscopic ASR gel; at the same time microcracks can be observed. In images taken at 74 days, crystalline hydrated structures are observed growing mainly in the voids. Additionally, the hybrid fibers tend to agglomerate, preferring to localize in less dense areas where finer aggregates are found. The solid line circle indicates the bundle of hybrid

fibers, the dashed line circle indicates a void filled with ASR gel, the dotted line circle indicates a dissolved aggregate, and the arrows show cracking aggregates. Finally, the dotted squares indicate the areas from which 3D volumes were rendered for each of the composite mortars; see Fig. 13.

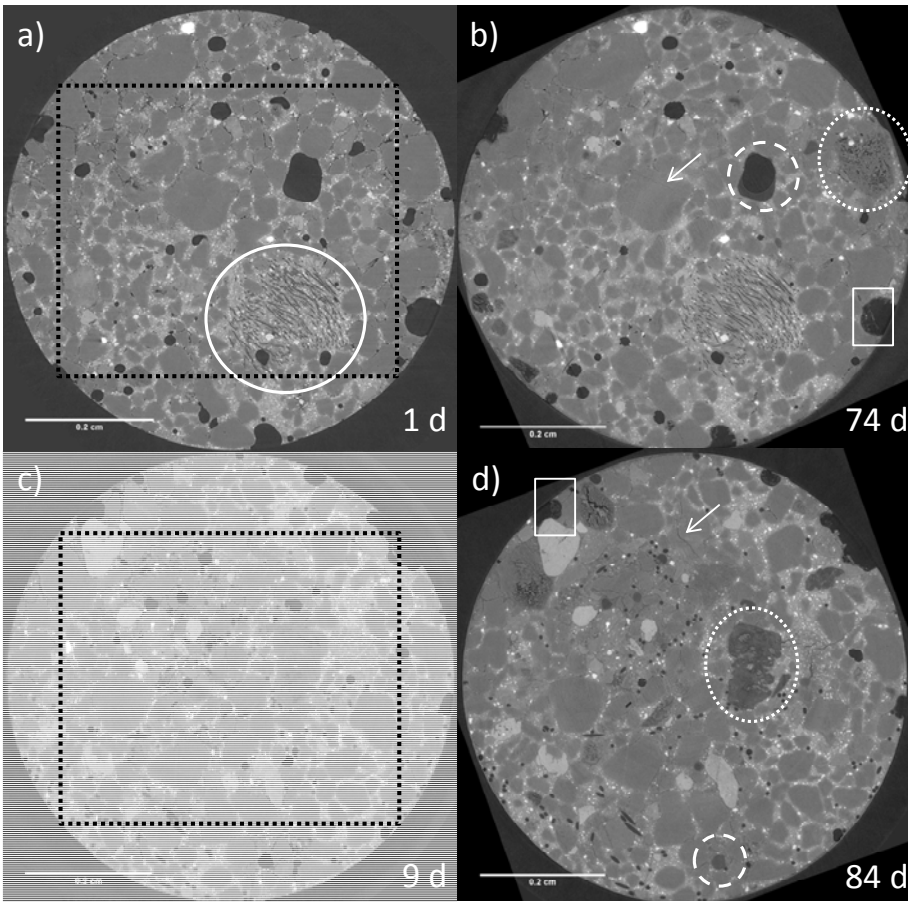

Fig. 12: Tomographic images taken from the PP and hybrid mortar composite cylinders after being immersed in 1M NaOH solution. Images (a) and (b) correspond to the hybrid fibers, while images (c) and (d) correspond to the PP cylinder. Scale bar represents 2mm.

The 3D images illustrated in Fig. 13, confirm the preferred distribution for each type of fiber, a bundled distribution for the hybrid fiber and the more uniform distribution of PP

Deleted: s

fiber. This bundling behavior can be related to the aspect ratio of the fibers and to the fact that the hydrophilic coated polymers may prefer the less dense, water rich areas, to the denser regions. The carboxylate groups of the EAA may be helping bridge this issue, being ionized by the high pH of the mixing and would prefer to adsorb and, therefore, reduce the materials incompatibility between the low density of the fibers and the denser inorganic hydrating cement paste. Future studies to evaluate hydrophilic polymer fibers with different aspect ratios to determine if the hydrophilic fibers are aiding or hindering dispersion would be valuable in interpreting these findings..

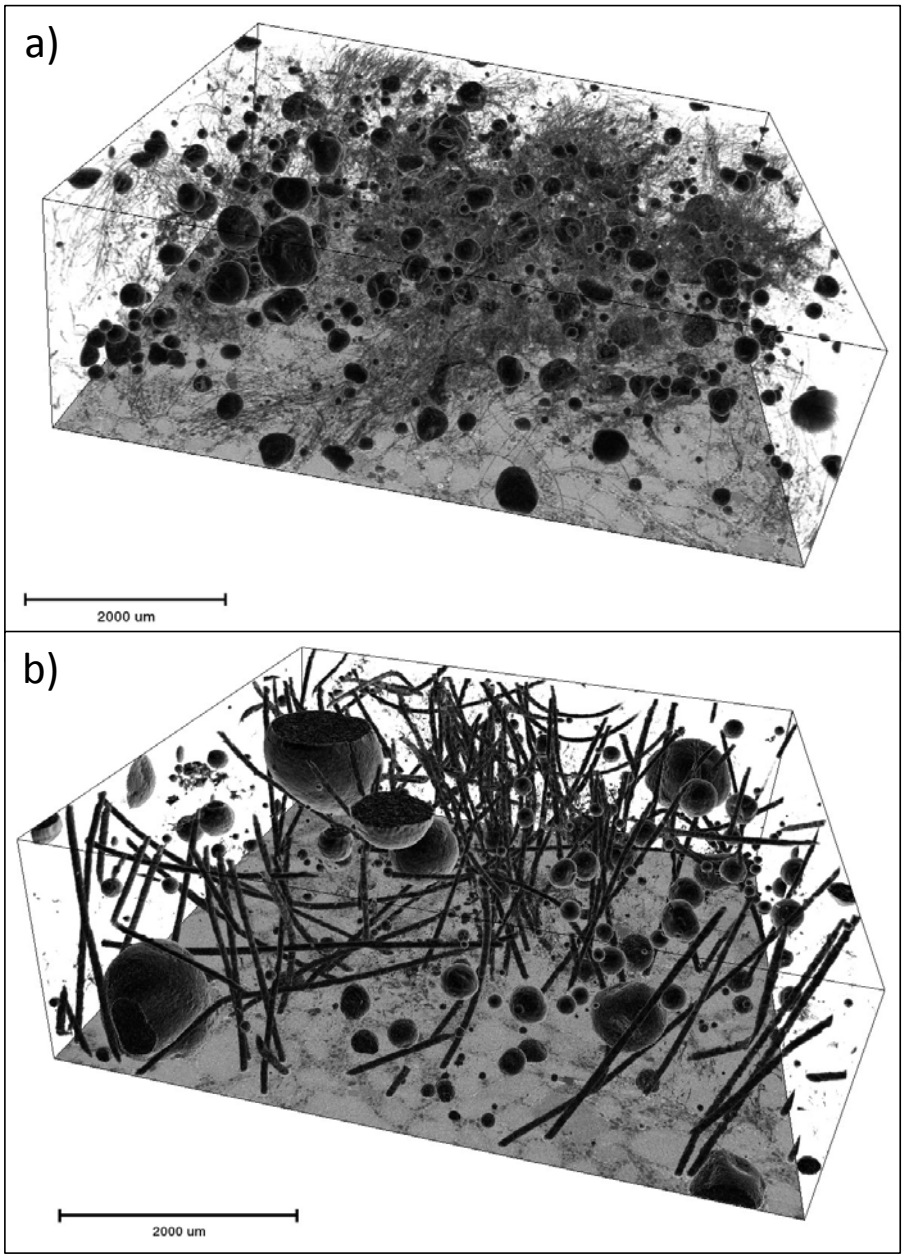

409

410 Fig. 13: 3D images showing fiber distribution in a cement mortar: (a) hybrid fiber block,
411 and (b) PP fiber block. Scale bar represents 2mm.

412

3.2.3. Flexure tests

To determine how the fibers improved the flexure response of the cement composites, third-point loading tests were conducted (Fig. 14). The beams with hybrid fibers stabilized at a higher post-cracking load (~290 kgf) compared to the beams with PP fibers (~140 kgf). After the initial flexure tests, it was observed that the hybrid fibers had not dispersed throughout the sample, tending to stay bundled in a configuration similar to that before mixing (Fig. 15).

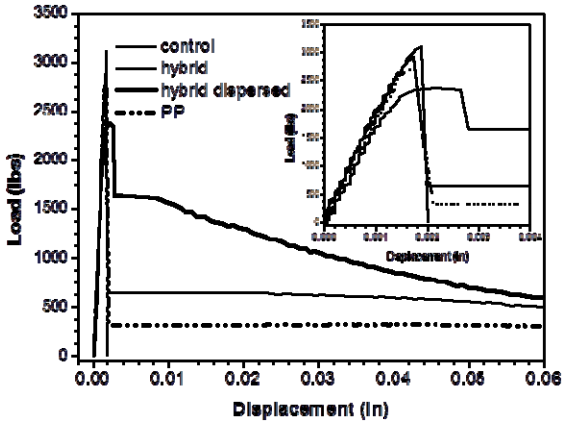

Fig. 14: Displacement behavior of beams with applied third-point loading. Inset is an enlargement at the breaking point.

Fig. 15a shows the PP fibers fairly evenly dispersed, and Fig. 15b shows the bundled hybrid fibers. Note how the bundles of hybrid fibers are still white, indicating that they were not coated in cement paste but remained bundled together throughout mixing and placing of the mortar. Consequently, a second set of beams was cast where the hybrid fibers were pre-dispersed by putting the fibers in a rigid container into which high pressure air was blown into one hole while being allowed to escape out another. The resulting fibers were very well dispersed. As shown in Fig. 13 the beams with pre-dispersed hybrid fibers stabilized at a significantly higher load upon cracking (~ 750 kgf). Likewise, Fig 15c shows that although the hybrid fibers did rebundle to some extent during mixing, the fibers were coated in cement paste during mixing (as evidenced by their gray appearance). The hybrid fibers did have a very thin diameter compared to their length, which promotes bundling

434 during mixing. The difference in aspect ratios between the PP and hybrid fibers was an
435 experimental limitation and certainly contributes to the differences in response.

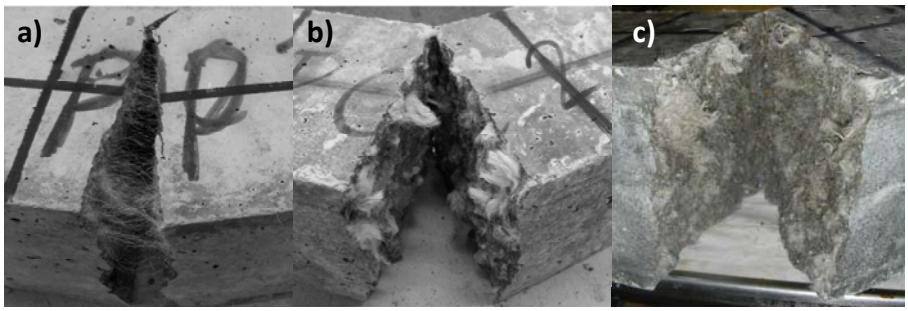

436

437 Fig. 15: Composite beams after completing the flexure tests: (a) PP fiber, (b) hybrid fiber,
438 and (c) pre-dispersed hybrid fibers.

439

440 **4. Conclusions**

441 This experimental study mainly focused on quantifying the chemical interaction between a
442 hybrid fiber and hydrated cement paste (HCP) by means of scanning transmission X-ray
443 microscopy (STXM). The coextruded hybrid (bi-component) fiber, consisted on an
444 ethylene acrylic acid copolymer (EAA) coaxially extruded with (polypropylene) PP core
445 fiber was analyzed and it´s near edge X-ray absorption fine structure (NEXAFS) was
446 obtained. Spectra from PP and EAA raw materials were obtained and helped to differentiate
447 the chemical signatures between them when incorporated into a coextruded hybrid fiber and
448 when this fiber was incorporated into a HCP matrix. This difference consisted of a splitting
449 in the peak at 287.7 eV, which is due to the carboxyl groups found in the EAA molecular
450 structure. Furthermore, Ca traces were found in the 1.7 µm EAA sheath, whereas, it was
451 not possible to find similar results when observing monofilament PP fibers that were in the
452 HCP. This could indicate the carboxyl groups in EAA improved the chemical bonding with
453 the HCP, although it was not possible to determine the Ca compound, due to the weak
454 spectra signal. Additionally, a microtomography (µCT) study was carried out on mortar
455 cylinders exposed to ASR attack for ~7days, which allowed quantification of the fiber
456 distribution, the aggregate dissolution, and the ASR gel formation. Finally, flexure tests

showed a significant increase in the toughness and post-cracking stabilized load carried by beams made with pre-dispersed hybrid fibers compared to the beams made with PP fibers. This improved mechanical response may at least, in part, be explained by the improved fiber-HCP bond that forms as a result of the hydrophilic carboxyl groups of the EAA fiber sheath bonding with Ca from the HCP.

Acknowledgments

C.W. Hargis was supported by the Berkeley Fellowship for Graduate Study and the Carlson-Polivka Fellowship. The authors want to acknowledge Tony Warwick for all his support at the Advanced Light Source. The Advanced Light Source is supported by the Director, Office of Science, Office of Basic Energy Sciences, of the U.S. Department of Energy under Contract No. DE-AC02-05CH11231.

References

1. Su Z, Bijen JMJM, Larbi JA. Influence of polymer modification on the hydration of portland cement. Cem Concr Res 1991; 22:242-50.
2. Shi L, Liu Jianzhong, Liu Jiaping. Effect of polymer coating on the properties of surface layer concrete. Chinese Materials Conference, Procedia Engineering 2011; 27:291-300.
3. Silva Da. Roman HR, Gleize PJP. Evidences of chemical interaction between EVA and hydrating Portland cement. Cem Concr Res 2002; 32:1383-90.
4. Betioli AM, Gleize PJP, John VM, Pileggi RG. Effect of EVA on the fresh properties of cement paste. Cem Concr Compos 2012; 34:255-60.
5. Raithby KD, Galloway JW, Williams RIT. Polypropylene-reinforced cement composites for surface reinforcement of concrete structures. Int J Cem Compos Lightweight Concr 1981; 3 (4): 237-46.
6. El Debs MK, Naaman AE. Bending behavior of mortar reinforced with Steel meshes and polymeric fibers. Cem Concr Compos 1995; 17:327-338.
7. Akihama S, Suenaga T, Banno T. The behavior of carbon fibre reinforced cement composites in direct tension. The Int J Cem Compos Lightweight Concr 1984; 6(3):159-68.
8. Di Maggio R, Franchini M, Guerrini G, Poli S, Migliaresi C. Fibre-matrix adhesion in fibre reinforced CAC-MDF composites. Cem Concr Compos 1997; 19:139-47.
9. Pakravan HR, Jamshidi M, Latifi M, Pacheco-Torgal F. Cementitious composites reinforced with polypropylene, Nylon and Polyacrylonitile fibers. VI International Materials Symposioum (Materiais 2011) – XV Meeting of SPM- Sociedade Portuguesa de Materiais 2011.
10. Larson BK, Drzal LT, Sorousian P. Carbon fibre-cement adhesion in carbon fibre reinforced cement composites. Compos 1990; 21(3):205-15.
11. Xu B. Toutanji HA, Gilbert J. Impact of resistance of Poly(vinyl alcohol) fiber reinforced high-performance organic aggregate cementitious material. Cem Concr Res 2010; 40:347-51.
12. Feleklglu B, Tosun K, Baradan B. Effects of fibre type and matrix structure on the mechanical performance of self-compacting micro-concrete composites. Cem Concr Res 2009; 39:1023-32.
13. Currie B, Gardiner T. Bond between polypropylene fibers and cement matrix. The Int J Cem Compos and Lightweight Concr 1989; 11(1):3-10.
14. Bentur A, Midess S, Vondran G. Bonding in polypropylene fibre reinforced concretes. The Int J Cem Compos and Lightweight Concr 1989; 11(3):153-58.
15. Peled A, Guttman H. Treatmen of polypropylene fibers to optimize their reinforcing efficiency in cement composites. Cem Concrete Compos 1992; 14:277-85.
16. Pereira EB, Fischer G, Barros JAO. Effect of hybrid fiber reinforcement on the cracking process in fiber reinforced cementitious composites. Cem Concr Compos 2012; 34:1114-23.
17. Blunt J, Ostertag CP. Hybrid fiber reinforced concrete for use in dridge approach slabs, CBM-CI International Workshop 2007:415-422
18. Yi CK, Ostertag CP. Mechanical approach in mitigating alkali-silica reaction. Cem Concr Res 2005; 35:67-75.

19. Banthia N, Sheng J. Fracture toughness of micro-fiber reinforced cement composites. Cem Concr Comp 1996, 18:251-269.
20. Banthia N, Nandakumar N. Crack growth resistance of hybrid fiber reinforced cement composite. Cem Concr Comp 2003, 25:3-9
21. Myint Lwin M, Ahlstrom G, Dealing with ASR in Concrete Structures. FHWA, ASPIRE, 2012:46-47.
22. Bae S, Bayrak O, Jirsa JO, Klingner RE. Effects of alkali-silica reaction/delayed ettringite formation damage on behavior of deeply embedded anchor bolts. ACI Structural J 2009:848-857.
23. Humphreys MF. The use of polymer composites in construction. International Conf. on Smart and Sustainable Built Environment, 2003: http://eprints.qut.edu.au/139/
24. Feiteira J, Ribeiro MS. Polymer action on alkali-silica reaction in cement mortar. Cem Concr Res 2013 (44): 97-105.
25. Juenger MCG, Lamour VHR, Monteiro PJM, Gartner EM, and Denbeaux GP. Direct observation of cement hydration by soft X-ray transmission microscopy. J Mat Sci Letters 2003; 22:1335-1337.
26. Hargis CW, Kirchheim AP , Monteiro PJM, Gartner EM. Early age hydration of calcium sulfoaluminate (synthetic ye'elimite, $C_4A_3\bar{S}$) in the presence of gypsum and varying amounts of calcium hydroxide. Cem Concr Res in press.
27. Silvia DA, Monteiro PJM. The influence of polymers on the hydration of portland cement phases analyzed by soft X-ray transmission microscopy. Cem Concr Res 2006; 36(8):1501-07.
28. Ha J, Chae S, Chou KW, Tyliszczak T, Monteiro PJM. Effect of polymers on the nanostructure and on the carbonation of calcium silicate hydrates: a scanning transmission X-ray microscopy study. J Mater Sci 2012; 47:976-89.
29. Reddy HP, Pyzik AJ, Morgan TA, Allen SM, Shinkel NM. Plastic fibers for improved concrete. US Patent 6,844,065 B2, 18 January 2005.
30. Bluhm H, Andersson K, Araki T, Benzerara K, Brown GE, Dynes JJ, Ghosal S, Gilles MK, Hansen HCh, Hemminger JC, Hitchcock AP, Ketteler G, Kilcoyne ALD, Kneedler E, Lawrence JR, Leppard GG, Majzlam J, Mun BS, Myneni SCB, Nilsson A, Ogasawara H, Ogletree DF, Pecher K, Salmeron M, Shuh DK, Tonner B, Tyliszczak T, Warwick T, Yoon TH. Soft X-ray microscopy and spectroscopy at molecular environmental science beamline at the Advanced Light Source. J Electron Spectroscopy and Rel Phenom 2006; 150:86-104.
31. Dhez O, Ade H, Urquhart SG. Calibrated NEXAFS spectra of some common polymers. J of electron Spectroscopy and Rel Phenomena 2003; 128: 85-96.
32. Image and spectra visualization and analysis, http://unicorn.mcmaster.ca/aXis2000.html
33. Hargis CW, Juenger MCG, Monteiro PJM. Aggregate passivation: lithium hydroxide aggregate treatment to suppress alkali-silica reaction. ACI J Mater in press.
34. ASTM C1260-07. Standard test method for potential alkali reactivity of aggregates (mortar-bar method). ASTM International, West Conshohocken, PA, 2007, 5 pp.
35. ASTM C1609-05. Standard test method for flexural performance of fiber-reinforced concrete (using beam with third-point loading. ASTM International, West Conshohocken, PA, 2005, 8 pp.
36. Topographic reconstruction analysis, http://www.octopusreconstruction.com/octopus

559 37. Image visualization and analysis, http://fiji.sc
560 38. Image visualization and analysis http://vsg3d.com

DISCLAIMER